8-2014

Magnetoviscous Effects of Magnetized Particle Threads in Magnetized Ferrofluid

Alexander Francis Cali
Montclair State University

Recommended Citation

Abstract

The magnetoviscous effect of applied fields on ferrofluids has been utilized in many applications in which the ferrofluid must remain in a fixed position while this effect on ferrofluids in motion has yet to be rigorously explored. In light of potential biomedical applications such as drug targeting, experiments were conducted to probe the rheology of ferrofluids on the micrometer scale. A non-conducting glass sphere of diameter 550 μm is dropped into a cylindrical container of magnetized ferrofluid of inner diameter 5.2 mm. This was repeated for two applied field strengths (980 gauss and 480 gauss) and over multiple angles with both a 4:1 diluted ferrofluid and a 4:1 diluted ferrofluid that had the larger particles removed (purified). Data from dilute ferrofluid show an angle-dependent in magnetized ferrofluid where maximal drag is attained when the applied field and the direction of the falling sphere are perpendicular to each other. This angle-dependence was not present in the purified ferrofluid which displayed a near-constant drag across all angles. These two results indicate that the main component of the drag experienced in the magnetized ferrofluid is due to the formation of magnetized particle threads within the ferrofluid and that large-diameter particles are responsible for this thread formation. A mathematical model was developed that formulates the drag as a fluid interaction between the array of threads within the ferrofluid and the Stokes flow due to the falling sphere. The model captures the angle-dependence seen in the experiments. The model results for falling spheres of multiple radii in a cylinder are qualitatively similar to those of uniform flow in a cylinder, implying that relative drag increases are mainly dependent upon sphere radius and negligibly affected by flow profile and wall effects.

MONTCLAIR STATE UNIVERSITY

Magnetoviscous Effects of Magnetized Particle Threads in Magnetized Ferrofluid

by

Alexander Francis Cali

A Master's Thesis Submitted to the Faculty of

Montclair State University

In Partial Fulfillment of the Requirements

For the Degree of

Master of Science

August 2014

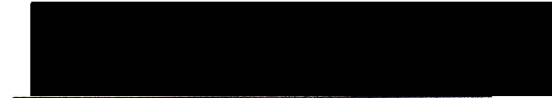College of Science and Mathematics

Department of Mathematical Sciences

Certified by:

8/28/2014

Date

Thesis Committee:

Thesis Sponsor: Philip Yecko
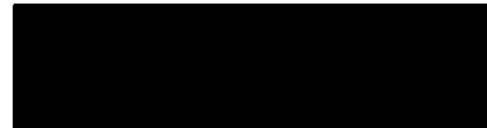
Committee Member: David Trubatch

Committee Member: Ashwin Vaidya

Committee Member: Eric Forgoston

ii

Magnetoviscous Effects of Magnetized Particle Threads in Magnetized Ferrofluid

A THESIS

Submitted in partial fulfillment of the requirements

for the degree of Master of Science

by

Alexander Francis Cali

Montclair State University

Montclair, NJ

2014

Acknowledgments

I would also like to thank my family and my friends. My family has always stood behind me and helped me when I needed them the most and without their love and support this thesis would not exist. My friends are responsible for reducing the stress of writing a thesis through their conversations, both serious and not, and helping me take a step back when I was too absorbed by my thesis to be able to write effectively.

Contents

List of Figures

1 Introduction

Ferrofluids are colloidal suspensions of magnetic nanoparticles dispersed throughout a liquid medium. In the presence of an applied magnetic field, the magnetic nanoparticles will tend to align with the magnetic field lines while the bulk fluid maintains its fluid properties. Ferrofluids, as opposed to other magnetic fluids, are characterized by a lack of sedimentation over time due to the size of the particles. Nanoparticles are approximately 10 nm in diameter which is small enough to be noticeably affected by the Brownian motion of the fluid itself. The Brownian motion is aided by the addition of a surfactant, a bi-polar organic molecule that adsorbs to the nanoparticles, which increases the effective radius of the nanoparaticles through steric repulsion, which is a repulsive force between two objects with interfering electron clouds. Brownian motion and surfactant work to keep the nanoparticles from interacting magnetically with each other, decreasing the formation of aggregates that may settle out of the suspension, even when exposed to magnetic fields, although long-time exposure to high-strength applied fields will cause particle aggregates to appear.

1.1 Ferrofluid Applications

The magnetic properties of ferrofluids make them uniquely ideal for many industrial applications. Many of these classical applications of ferrofluids are fixed-position applications where magnetic fields are utilized to hold the ferrofluid into place. An early such application of ferrofluids is being used as sealants for rotary shafts such as those found in the harddrives of computers [1, 2]. Since the harddrive is spinning, using a solid to act as a seal would lead to friction, heating, and warping of the involved materials. A small application of ferrofluid between the spinning harddrive and the shaft is all that is needed to seal the harddrive from unwanted debris because

the ferrofluid maintains its ability to flow, even when its viscosity is increased by the magnetic field of the harddrive.

Ferrofluid is also used as passive heat dissipation in audio speaker systems [1, 2]. Ferrofluid is placed in the gap that allows the voice coil to vibrate. As the voice coil is supplied electricity and begins to vibrate, a large amount of heat is generated. The magnetic properties of the ferrofluid allow this heat to be quickly dissipated. As the ferrofluid is heated the Brownian motion of the carrier fluid begins to increase, decreasing the magnetism exhibited by the magnetic nanoparticles due to thermal agitation. Particles from a cooler section of the ferrofluid are now more magnetized than the nanoparticles in the hotter part of the ferrofluid closer to the voice coil and a natural convection current is created to help keep the voice coil cool.

1.2 Motivation

More contemporary applications of ferrofluids are moving away from the fixed-position applications discussed above. Instead many biomedical applications are being developed. Ferrofluids can act as magnetic resonance imaging (MRI) contrast agents. Ferrofluids have different magnetic relaxation times than the surrounding tissue when subjected to the magnetic pulses of the MRI machine and can enhance the clarity of the image when introduced to the body.

Among the most current biomedical applications is drug targeting [1, 2, 3, 4]. Drug targeting uses the ferrofluid's magnetic attraction to guide it through the body to a particular location before fixing it in place. The development of techniques making drug targeting with ferrofluids a viable option would have a powerful impact in the medical world. Globally damaging treatments such as chemotherapy would no longer be introduced systematically to deal with isolated problems within the human body.

The issue arises in that there is ferrofluid being guided through the bloodstream.

There is no way of knowing exactly how it is going to travel from the injection site to the target site. While the ferrofluid is navigating the bloodstream the direction of the applied field will not be constant, which implies that there will be a variable viscosity to the ferrofluid while it is in transit. It is also not experimentally known how the magnetoviscosity of a ferrofluid changes with applied field direction, although theoretical models do exist. How is the ferrofluid going to respond to the natural flow of the bloodstream and the time-dependent applied field angle? The only way to explore what is going on inside the ferrofluid is through direct numerical simulation.

2 Background

In order to explore the magnetoviscous response of magnetized ferrofluid in the scope of drug targeting applications one must understand how diluting ferrofluid affects its internal structure. Ferrofluids are designed so that the magnetic nanoparticles interact minimally. Dilution of a ferrofluid alters the volume ratio of surfactant to carrier fluid and magnetic nanoparticles to carrier fluid and the consequences must be explored.

2.1 Magnetism

The magnetic moment of a substance is a measure of how responsive a substance will be when exposed to an applied magnetic field. When an atom is in the presence of an applied magnetic field the electrons will tend to orient themselves so that their magnetic moments are aligned with the applied field, creating a magnetic moment in the aforementioned macroscopic object.

2.1.1 Magnetization

In substances that consist of multiple magnetic moments, such as ferrofluids it can be useful to employ the use of a bulk property, magnetization. The magnetization of a substance is

$$\boldsymbol{M} = \frac{\boldsymbol{m}}{V} \tag{1}$$

where $\boldsymbol{M}$ is the magnetization of the substance, $\boldsymbol{m}$ is the magnetic moment, and V is the volume [5]. When an imposed field acts on a magnetizeable substance, each of the magnetic moments try to orient themselves with the applied field which requires time. Ferrofluids have a low volume concentration of magnetic particles and the time required for particles in motion to orient themselves is on the order of 10^{-6} s and is considered neglible.

2.2 Magnetic Fluids

There are two different types of magnetic fluids: ferrofluids and magnetorheological fluids (MR fluids). The main difference between these two magnetic fluids is that MR fluids have magnetic particle diameters on the order of 1 μm as opposed to 10 nm. This increased particle diameter is enough for the magnetic forces to dominate the thermal forces and form aggregates of magnetic particles, referred to as magnetic particle threads. These threads cause the MR fluid to become rigid and unable to flow under an applied field until a force larger than some threshold value, the so-called yield stress, is applied. Ferrofluids, on the other hand, do not have average particle diameters large enough for the magnetic forces to dominate thermal forces which allows ferrofluids to maintain their ability to flow due to the absence of these particle threads.

2.2.1 Magnetoviscosity

Magnetoviscosity refers to the changes in a magnetic fluid's viscosity caused by an applied magnetic field. Magnetoviscous effects in ferrofluids vary based upon magnetic nanoparticle volume fraction, size, and distribution, as well as applied field strength. In standard ferrofluids, magnetic nanoparticles are generally non-interacting and exhibit vorticity-induced magnetoviscous increases. When a ferrofluid is diluted the magnetic nanoparticles are able to interact magnetically and form macro-structures within the ferrofluid causing yield stress related magnetoviscous increases. In both magnetoviscous effects, the increase in viscosity can be viewed as a direct consequence of increased flow resistance or increased drag on the magnetic nanoparticles and macro-structures.

2.2.1.1 Vorticity-induced Models

The Shliomis model for magnetoviscosity is a vorticity-induced model [6]. In the presence of an applied magnetic field the magnetic moment of the magnetic nanoparticles will align themselves with the applied field. If the vorticity and the applied field are misaligned then there will be a tendency of the flow to try to rotate the particle in a way that the magnetic moment will no longer point in the direction of the applied field. This competition between the vorticity and the magnetic moment greatly hinders the particles' movement which leads to an increase in the effective viscosity of the fluids as depicted in figure 1.

This is a theoretical model that assumes all particles are non-interacting. This effect is not the dominant effect in the problem addressed in this thesis. Models exist that theoretically predict small particle interactions [7]. This model predicts that small chains of magnetic nanoparticles can form due to the electromagnetic attraction between particles. The model suggests that chains of up to 5 to 7 nanoparticles may form one-particle thick chains. Due to the small sizes of these structures they create
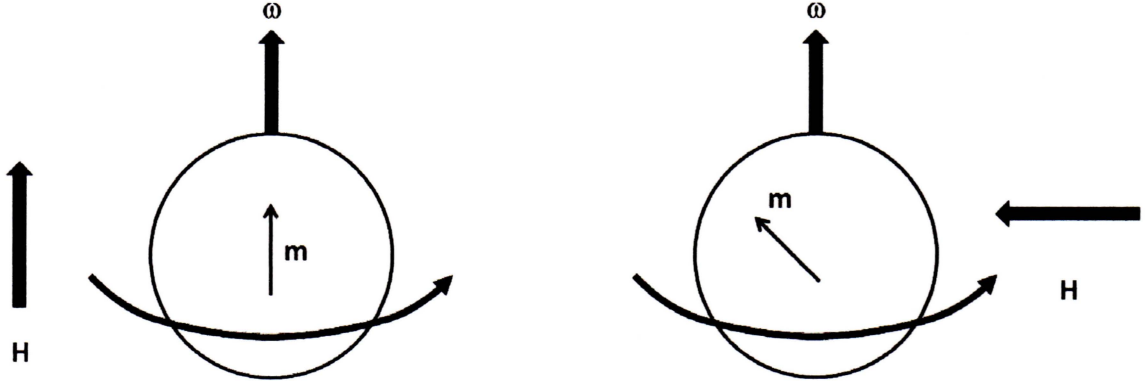
Figure 1: The misalignment of the vorticity, ω and applied field, $\boldsymbol{H}$ cause a torque that acts on the magnetic moment, $\boldsymbol{m}$, hindering the particle movement, effectively increaseing the ferrofluid's viscosity.

the same effect as the single, non-interacting particles in the Shliomis model.

2.2.1.2 Thread-induced Models

Ferrofluids, while manufactured with a mean particle diameter, are not exactly mono-disperse. Particles with the largest diameters have magnetic moments large enough to dominate the Brownian forces of the carrier fluid and the steric repulsion of the surfactant. These particles have the ability to form macro-structures within the fluid that are thousands of particles in diameter and span the experimental space, despite the inability of the particles of mean diameter to do so [8]. Zubarev et al. show that a model that predicts the formation of structures within a ferrofluid based upon the concentration of only the largest particles agrees with experimental observations [9]. The mechanism for the existence of a yield stress in this model is the destruction of any thread-like structures that form as a result of shear forces.

Zubarev et al. also show that under the assumption of small chain-like aggregates bridging gaps in magnetic suspensions, experimental observations are validated. Two important parameters involving magnetic fluids are the dimensionless parameters

$$\lambda = \frac{\mu_0}{4\pi} \frac{\boldsymbol{m}^2}{d^3 kT} \tag{2}$$

which is a ratio of magnetic forces to Brownian forces where μ_0 is the permeability of free space, m and d are the magnetic moment and diameter of a magnetic nanoparticle respectively, k is the Boltzman constant which relates a particle's energy with its temperate, and T is the absolute temperature of the ferrofluid, and the Mason number

$$Mn = \frac{72\eta_0\dot{\gamma}}{\mu_0\alpha\boldsymbol{H}^2} \tag{3}$$

which is a ratio of shear rate to magnetic forces where η_0 is the viscosity of the fluid when not exposed to a magnetic field, $\dot{\gamma}$ is the shear rate of flow, α is a parameter comparing the relative permeabilities of the magnetic nanoparticles and the carrier fluid, and $\boldsymbol{H}$ is the applied magnetic field [10]. An experimental observation for magnetic suspensions with large values of λ is

$$\frac{\eta}{\eta_0} - 1 \propto Mn^{-\Delta} \tag{4}$$

where η is the effective viscosity of the magnetic suspension under the effects of an applied magnetic field and Δ is an exponent describing the proportionality [10]. In theoretical investigations of this relationship, λ is taken to be large and Δ is determined to be a fixed value of 1, not varying with applied field strength or the volume fraction of magnetic particles. Experimental investigations of this value find Δ to be within the range $\frac{2}{3} \leq \Delta \leq 1$. It is also shown that when λ is not assumed to be very large, there is a dependence on volume concentration where higher values of Δ are associated with higher values of volume concentration when the parameter λ is small [10].

2.3 Structures

2.3.1 Experimental Verifications

The mechanism by which magnetic nanoparticles aggregate is poorly understood. While it is accepted that small 5 to 7 nanoparticle micro-structures may form in ferrofluids, the formation of larger macro-structures that are thousands of nanoparticles in diameter with lengths greater than a millimeter has not previously been seen in bulk ferrofluid. These macro-structures are seen to form primarily in diluted ferrofluid samples, not in standard samples. Magnetoviscous effects explainable by thread-like macro-structures within ferrofluids have been reported for dilutions of up to 10:1 [4].

Experimental verification of threading has been reported through small angle neutron scattering [11, 12]. Small angle neutron scattering involves directing a beam of neutrons at a sample and recording the amount of neutrons scatterred at each angle. In [11, 12], ferrofluids are subjected to multiple magnetic field strengths and various shear rates. At low field strengths and low shear rates, structures were visualized but were quickly lost when the shear rates were increased. In high field strengths and low shear rates little was seen until the shear rates were increased and the structures moved and became visible.

Ferrofluids are designed not to form threads. It is only in ferrofluids that have been diluted that these threads are seen to form. The particles that form the threads in diluted ferrofluids are reported to have a much higher concentration of large-diameter magnetic particles than the original fluid, indicating that the threads are formed through interparticle forces between the larger particles in the ferrofluids [13, 14]. Large particles were removed from the ferrofluid through magnetic separation and comparison of the two fluids' reactions to applied magnetic fields demonstrated a stronger magnetoviscous effect in the fluid with larger magnetic nanoparticles.
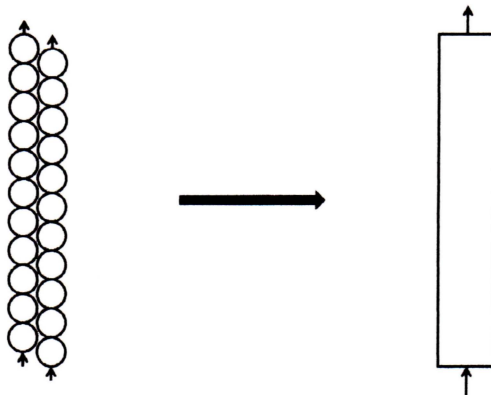
Figure 2: Magnetic particle threads consist of many individual magnetic nanoparticles, each with their own magnetic moment. The thread on the left with n magnetic particles of magnetic moment, $\boldsymbol{m}$, can be viewed as a single object of volume, V, and magnetization, $\boldsymbol{M}$.

2.3.2   Thread Formation

Structures are the result of large-diameter particles interacting with each other but the actual formation of these threads has not been visualized. The proposed mechanism of this threading is magnetic dipole interaction of the larger nanoparticles in the ferrofluid. As magnetic substances can be described by their magnetization, equation (1) indicates that the magnetic moment of a particle is proportional to its volume. In the case of thread formation, larger particles will have a much larger magnetic moment. This will lead to much greater attraction between larger particles which will cause them to aggregate. By equation (1) particle aggregates can also be treated as their own object with one magnetic moment as in figure 2. This implies that aggregation increases the effective magnetic moment and increases the attraction towards other particles leading to a cascading effect, creating larger structures within the ferrofluid.

The structures take the forms of threads as opposed to other shapes because any two nanoparticles cannot be directly next to one another. Two nanoparticles with
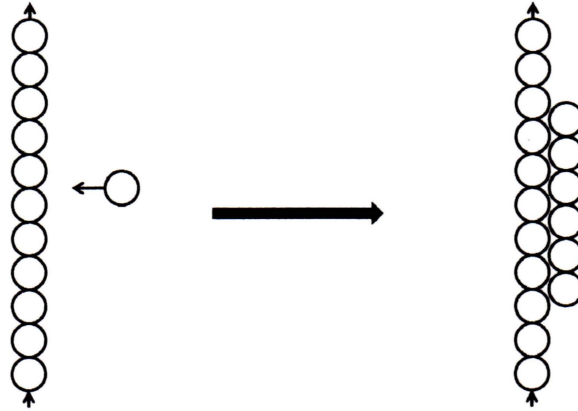
Figure 3: Magnetic dipole interactions favor the creation of long, single particle chains. However, sufficiently long chains can attract single particles in a staggered fashion, leading to the formation of three-dimensional threads.

parallel moments side-by-side will have the north and south poles aligned as well. This will lead to a mutal repulsion by each particle on the other. It is more energetically favorable for the particles to align in a staggered fashion where a nanoparticle will settle in between two nanoparticles attracted "head-to-tail" as in figure 3. In the case of two threads formed in different locations of the ferrofluid, they too will repel each other as did two magnetic spheres for identical reasons.

2.3.2.1   Mobility Model

One explanation for why threads only form in dilute samples of ferrofluids is due to an increase in particle mobility [8]. Operating within the Stokes regime, characterized by small-scale, low-velocity, viscous flows, the constant motion of the magnetic nanoparticles within the ferrofluid creates local flows around each moving particle. When ferrofluid is exposed to an applied field each of the magnetic nanoparticles will attempt to align themselves with the applied field. This alignment is hindered in standard ferrofluid because there are so many particles, each creating their own local flow. Each time a particle encounters a local flow its motion is disrupted, altering the direction of the particle's magnetic moment and making it more difficult for alignment to occur as in figure 4. In diluted ferrofluid the concentration of magnetic nanoparti-

(a) Standard nanoparticle motion   (b) Diluted nanoparticle motion
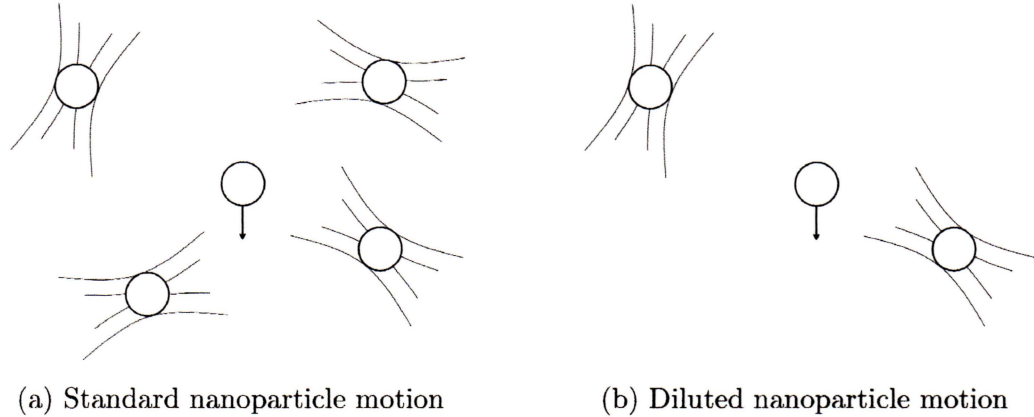
Figure 4: There is a flow associated with each moving particle. As any one particle travels through another's local flow it is mechanically effected and redirected away from its original path. In non-diluted ferrofluids with many more magnetic particles present, there are more local flows that act against particle aggregation.

cles is smaller and as a result there are less local flows that need to be navigated by each particle. As a result it is easier for particles to align themselves with the applied field and for structures to begin to form.

2.3.2.2   Surfactant Model

Another model for particle aggregation is in diluted ferrofluids is related to the amount of surfactant in the ferrofluid [15]. The surfactant model takes into account that upon dilution the volume ratio of surfactant in the ferrofluid is reduced as depicted in figure 5. There is an equilibrium of surfactant that is adsorbed onto the nanoparticles and free surfactant that is in the ferrofluid. When the amount of free surfactant is reduced, adsorbed surfactant will detach from the particles until an equilibrium is again reached. Less surfactant coating each particle and dispersed throughout the ferrofluid weakens the steric repulsion between particles which causes magnetic forces between particles to be more efficient.

(a) Standard surfactant equilibrium   (b) Diluted surfactant equilibrium
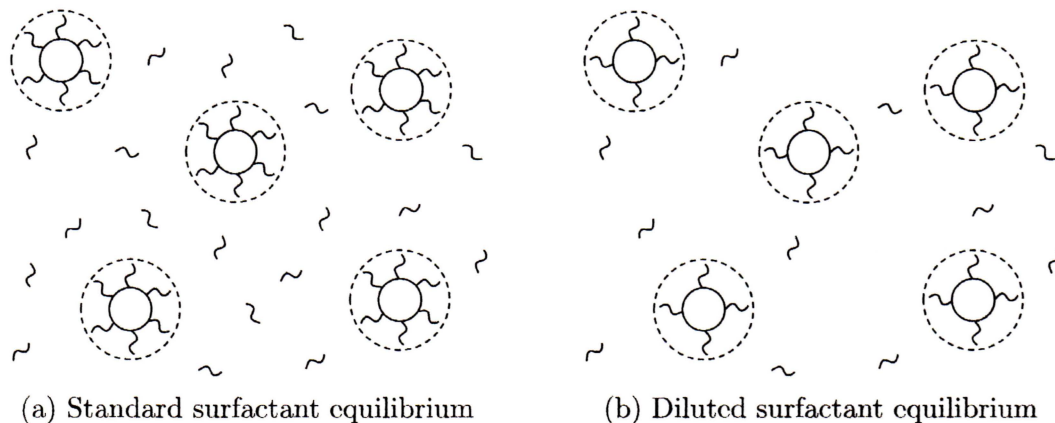
Figure 5: Dilution of ferrofluid allows aggregates to form due to the smaller volume fraction of surfactant in the ferrofluid. Less surfactant on the surface of the nanoparticles and spread out in the ferrofluid means less steric repulsion to balance the magnetic attraction.

2.4 Falling-sphere Rheometry

2.4.1 Stokes Flow

The governing equation for fluid motion is the Navier-Stokes equation. The Navier-Stokes equation takes the following form when dealing with incompressible fluids, such as ferrofluids,

$$\rho \left(\frac{\partial \boldsymbol{u}}{\partial t} + \boldsymbol{u} \cdot \nabla \boldsymbol{u} \right) = -\nabla p + \mu \nabla^2 \boldsymbol{u} + \boldsymbol{f} \tag{5}$$

where ρ is the fluid density, $\boldsymbol{u}$ is the fluid velocity, p is the pressure μ is the dynamic viscosity of the fluid, ∇^2 is the Laplacian operator, and $\boldsymbol{f}$ represents body forces acting on the fluid. Proper nondimensionalization shows that equation (5) can be further reduced to

$$\nabla p = \mu \nabla^2 \boldsymbol{u} \tag{6}$$

when dealing with small-scale, slow, viscous flows in the steady state where body forces are absent. This equation is also said to be valid when the Reynolds number, Re, of a flow approaches zero.

When equation (6) holds, the flows in question are often referred to as Stokes flows or creeping flows and are said to take place in the Stokes regime. To verify that the flows explored in the laboratory are in the Stokes regime, the Reynolds number must be calculated. The Reynolds number using experimental data is

$$Re = \frac{lU_0\rho}{\mu} = \frac{(550\text{x}10^{-6}m)(2.19\text{x}10^{-2}m/s)(1.21\text{x}10^3 kg/m^3)}{6\text{x}10^{-3}Pa \cdot s} \approx 2.43 \qquad (7)$$

where the chracteristic length scale, l, is the diameter of the falling sphere, the characteristic velocity, U_0, is the average flow speed for ferrofluid without an applied field present, and ρ and μ are the density and viscosity respectively of standard EFH1 as provided in [16]. This particular Reynolds number is computed using diluted EFH1 without an applied field present, and as such, is an upper bound on the Reynolds number for all flows in the experiment. Although 2.43 is not approaching zero, Stokes flow can be a useful approximation for Reyonolds numbers as high as 5 [17]. The assumption of Stokes flow is thus validated.

2.4.1.1   The Stokes Stream Function

When analysing axisymmetric flows, it is often beneficial to employ a stream function. A stream function will make the problem two-dimensional and creates a function that automatically satisfies the continuity equation of incompressible flows, $\nabla \cdot \boldsymbol{u} = 0$. A stream function plots the the streamlines of a flow which are tangential to the velocity at all points. A stream function in spherical coordinates is defined by

$$u_r = \frac{1}{r^2 \sin\theta} \frac{\partial\psi}{\partial\theta} \qquad (8)$$

$$u_\theta = -\frac{1}{r \sin\theta} \frac{\partial\psi}{\partial r} \qquad (9)$$

where u_r and u_θ represent the radial and angular components of the velocity vector field respectively.   The flow in the ferrofluid is driven by a falling sphere descending through the ferrofluid. The Stokes stream function is a well-known solution to Stokes flow around a sphere subject to the boundary conditions

$$\frac{\partial \psi}{\partial r} = \frac{\partial \psi}{\partial \theta} = 0 \qquad \text{when } r = a \tag{10}$$

$$\psi \to \frac{1}{2} U r^2 \sin^2 \theta \qquad \text{when } r \to \infty. \tag{11}$$

where equation (10) is the no-slip condition and equation (11) is the far-stream condition [18]. The far-stream condition implies that separation of variables may be used and that ψ is of the form

$$\psi = f(r) \sin^2 \theta. \tag{12}$$

The differential equation that governs the flow is

$$\left[\frac{d^2}{dr^2} - \frac{2}{r^2} \right]^2 f(r) = 0. \tag{13}$$

with a general solution of

$$f(r) = A\frac{1}{r} + Br + Cr^2 + Dr^4. \tag{14}$$

Applying the boundary conditions yields the Stokes stream function

$$\psi = \frac{1}{4} U \left(\frac{a^3}{r} - 3ar + 2r^2 \right) \sin^2 \theta. \tag{15}$$

2.4.1.2   Stokes Paradox

As there are also cylindrical structures in the problem to be solved, an exploration of Stokes flow around cylinders is warranted. Following a similar approach as in the previous section, but this time in cylindrical coordinates one arrives at the differential

equation

$$\left[\frac{d^2}{dr^2} + \frac{1}{r}\frac{d}{dr} - \frac{1}{r^2}\right]^2 f(r) = 0 \tag{16}$$

with a general solution of

$$f(r) = A\frac{1}{r} + Br + Cr\ln r + Dr^3 \tag{17}$$

and the following no-slip and far-stream boundary conditions

$$\psi = \frac{\partial\psi}{\partial r} = 0 \qquad \text{when } r = a \tag{18}$$

$$f(r) \propto Ur \qquad \text{when } r \to \infty \tag{19}$$

as given in [18]. Applying these boundary conditions to (17) sets all constant, $A = B = C = D = 0$. There is no stream function that satisfies simultaneously the no-slip condition and the far-stream conditions.

2.4.1.3 Oseen Length

In order to understand why this occurs one must return to the ratio of inertial forces to viscous forces and view this ratio at infinity. Typically the Reynolds number is

$$Re = \frac{\rho U_0 a}{\mu} \tag{20}$$

where a is the radius of the sphere. By defining a modified Reynolds number that looks beyond the radius of the sphere, a distance L from the center as opposed to just a,

$$Re^* = \frac{\rho U_0 L}{\mu}, \tag{21}$$
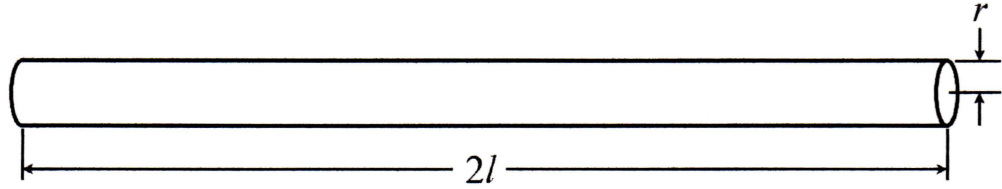
Figure 6: Schematic showing the relevant slender body theory dimensions, the cross-sectional radius, r, and the half-length of the cylinder, l. When $\frac{r}{l} \to 0$ then slender body theory can be applied.

one can see that Re^* grows without bounds as L increases. Rewriting this in terms of the real Reynolds number by multiplying and dividing by a one has

$$Re^* = \frac{\rho U_0 a}{\mu} \frac{L}{a} = Re \frac{L}{a}. \tag{22}$$

This implies that once $\frac{L}{a} > \frac{1}{Re}$, inertial forces are no longer negligible. This is refered to as the Oseen length. The Oseen length of this problem is

$$\frac{L}{a} >= \frac{1}{Re} = 0.412. \tag{23}$$

2.4.2   Single-Thread Theories

Experimental evidence in support of the existence of threads in diluted ferrofluids also suggest that the ratio of cross-sectional area to length is very small as in figure 6 [8, 11, 12]. Slender body theory is a theory for Stokes flows around objects in the limit that this ratio is zero. It has been shown that in this limit the drag force experienced by a slender body by Stokes flow perpendicular to the axis of symmetry is twice that of the force experienced by Stokes flow parallel to the axis of symmetry [19, 20].

2.4.3   Thread Arrays

Stokes flow through an array can be determined using multiple methods and assumptions. The first method assumes that the array through which the fluid flows

is a regular array. The symmetry of a regular array can be exploited to reduce the difficulty of the problem as there will only be a small number of different volume integrals to compute in order to determine the global flow through the array [21, 22].

The second method makes no assumptions about the shape of the array. Solving for the global flow through a random array can itself be solved multiple ways. One method solves for Stokes flow around a single body and assumes that the affect of the rest of the array be approximated as the resistance experienced by flow through a porous medium [23]. A second method for solving Stokes flow through random arrays involves using average quantities of the flow from random areas of flow [24]. This approach assumes that the volume fraction of array objects in any randomly chosen section of the fluid is the same as any other, and computes the average force of this chosen section of fluid on the remaining flow.

The third main method for analyzing Stokes flow through an array is the cell model [25, 26, 27]. While the previous approaches can work for any volume fraction of array to fluid, this method can only be used with a low volume fraction. The governing assumption is that the array objects are so far away from each other that the flow disturbance created by any one array object dies out before another array object is reached. Due to this a "cell" may be created around the array object such that the ratio of the volume of the array to the surrounding fluid is the same as the ratio for the entire flow. Boundary conditions are on the cell boundary instead of at infinity. As the flow around any one object does not affect any other, the solution for flow around this single object is approximately the same as for the global flow.

Using a combination of a cell model and porous media model, Happel demonstrates that both flows normal and tangential to the cylinder have a Kozeny constant associated with them [26]. The Kozeny constant is a parameter used to describe flows through porous media and is inversely proportional to the permiability of a porous medium. As such the Kozeny constant is a measure of much resistance a flow expe-

riences as it travels through a porous medium, or as in the case of this application, an array of threads. The Kozeny constants for tangential and normal flow through an array of threads are

$$
\begin{aligned}
k_t &= \frac{2\epsilon^2}{(1-\epsilon)[2\ln(\frac{1}{1-\epsilon}) - 3 - 4(1-\epsilon) - (1-\epsilon)^2]} \\
k_n &= \frac{2\epsilon^2}{(1-\epsilon)\ln(\frac{1}{1-\epsilon})\frac{1-(1-\epsilon)^2}{1+(1-\epsilon)^2}}
\end{aligned}
\tag{24}
$$

where k_t and k_n are the Kozeny constants of tangential flow and normal flow respectively and the parameter ϵ is the void fraction per unit volume of the flow, where large values represent small volume fractions of threads in the flow. In the limit where $\epsilon \to 1$ one finds that

$$
\begin{aligned}
k_t &\to \frac{1}{(1-\epsilon)\ln(\frac{1}{1-\epsilon})} \\
k_n &\to \frac{2}{(1-\epsilon)\ln(\frac{1}{1-\epsilon})} = 2k_t.
\end{aligned}
\tag{25}
$$

As can be seen, when the volume fraction of threads is small compared to the rest of the fluid, the Kozeny constant for normal flow is twice that for tangential flow, implying that the resistance met (drag force) by normal flow will be twice that of tangential flow. This indicates that just as is the case for a single thread, normal flow in an array of threads will experience twice the drag force as tangential flow.

2.4.4   Finite Domain

Each of the preceeding methods of determining the drag force on an infinitely long cylinder made assumptions of the flow at infinity where uniform flows went to zero or a mean velocity U_0 (ball frame or lab frame). This is true for the cell models as well, as the boundary of each cell is considered far enough away from the source of the disturbance that the flow is no longer affected. The experiment is conducted in a

23

finite container with a fluid interface at the top, and unknown or varying topography at the bottom. The finite nature of this experiment is important as drug targeting applications require flow through the circulatory system, which is comprised of cylindrical pathways of varying diameters and orientations in space.

3   Experiments and Data Analysis

The experiment involves dropping non-conducting spheres into tubes of magnetized ferrofluid. The magnetic field is applied over varies angles, α, to capture the drag anisotropy of the magnetized ferrofluid. The trajectories of the falling sphere are recorded and used to calculate the terminal velocity from which is it possible to compute the drag experienced by the sphere through the Stokes drag formula. For a sphere falling at a steady velocity through a fluid in Stokes regime, the Stokes drag formula is

$$F_{Stokes} = 6\pi \mu r U_0, \tag{26}$$

where μ is the viscosity of the ferrofluid in its magnetized state, r is the radius of the sphere, and U_0 is the terminal velocity of the sphere [28].

3.1   Equipment

All experiments were conducted at the XOR 32-ID beamline at the Advanced Photon Source in Argonne National Laboratory. Ferrofluid EFH1 from Ferrotec was placed inside plexiglass tubes of inner diameter, outer diameter, and height of 5.2 mm, 7.0 mm, and 10.4 mm respectively. These tubes of ferrofluid were placed in the center of two permanent magnets in the region of constant applied field as detailed by Peng et al. in [29]. Each set of magnets was held in place by a unique wooden brace to allow proper spacing and manueverability. Altering the angle of the applied field was done by tilting the brace and holding it in place with clay. A remote actuator was

utilized to push 500 μm diameter glass spheres into the tubes of ferrofluid. Images of the experimental setup can be seen in figures 7 and 8. 25 keV X-rays were used for imaging purposes and were converted to visible light by a 100 μm thick yttrium aluminum garnet scintillator. The motion of the glass sphere was recorded by a 500 frames per second high frame rate digital CMOS camera. Trajectories of the falling sphere were obtained by viewing the frames through freeware program ImageJ and used by Microsoft Excel to calculate the terminal velocity of the sphere.

3.2 Parameters

The trajectory studies were conducted over many different field angles, two different field strengths, and two different dilutions. The angles were chosen by tilting and fastening the magnetic setup in place and then measuring the angle with respect to the horizontal. This approach was chosen due to its time-efficiency. The magnetic setup was fixed in place using clay, making it difficult to fix the setup at precise, pre-chosen angles.

Two different magnetic setups were used throughout the experiment. Magnetic setup PermB has a 980 gauss magnetic field and the setup PermC has a magnetic field of 490 gauss. The effect of the different field strengths were recorded over multiple angles each although the only matching angles were 0 degress (horizontal) and 90 degrees (vertical) for reasons discussed above.

Two different types of dilution were used in this experiment. The first dilution was a 4:1 mixture of mineral oil to ferrofluid. This was originally done to aid visability of the ferrofluid interior as mineral oil has low opacity as opposed to the ferrofluid's oil-based carrier fluid. All data using this type of dilution are refered to as "diluted". The second type of dilution was motivated by experimental results to be discussed in section 4.1.1. This dilution was performed on the 4:1 diluted ferrofluid in a process refered to as "purification". Purified ferrofluid has had much many of the large-
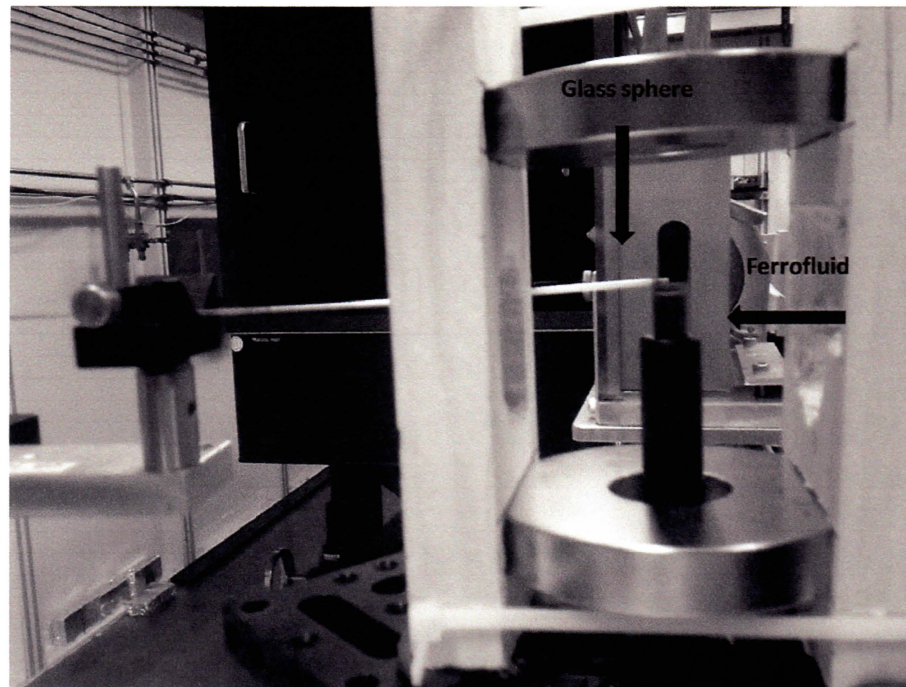
Figure 7: A labeled schematic of the experimental setup. Glass spheres are pushed out of a long tube using a remote actuator and the spheres fall into a small tube of magnetized ferrofluid.
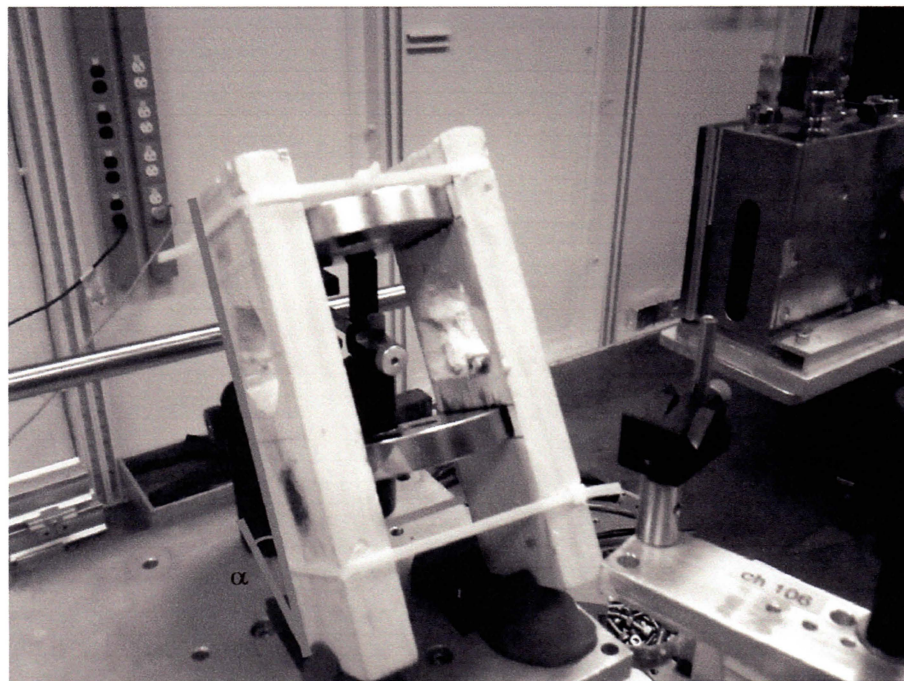
Figure 8: Rotated magnetic assembly is fixed in place using clay. The angle α is measured with respect to the horizontal.

diameter nanoparticles removed from the fluid, reducing the mean particle diameter of the fluid.

To purify a ferrofluid a powerful permanent magnet is placed at the bottom of a tube of ferrofluid. This attracts the larger particles to the very bottom of the tube while the smaller particles are closer to the top of the fluid. A syringe is used to draw out the ferrofluid and leave the larger particles at the bottom of the tube. This process is then performed a second time on the once-purified ferrofluid to ensure a large fraction of the large-diameter nanoparticles have been removed from the ferrofluid.

3.3   Data Collection and Analysis

The tiff image files were viewed using freeware program ImageJ. ImageJ was used to open all of the images and play it as a video with the frame number displayed. The first and last frame that approximately half of the sphere was visible were recorded with the final frame number being adjusted slightly so that the difference between the first and last frame number would be divisible by 10. The difference divided by 10 would be the step size to increment from the first frame to the last frame providing 11 frames from which to calculate the trajectory of each sphere A sample of 6 frames can be seen in figure 9.

The trajectories of the spheres were computed by choosing three points around the circumference of a circle and computing the coordinates of the intersection of the perpendicular bisectors of two lines created by the three points. Refer to figure 21 and appendix A for the details of how these coordinates were derived. After obtaining an equation for the midpoints of a circle based upon three points about its circumference, Microsoft Excel was used to plot the trajectories of the spheres. The trajectories were used to determine the terminal velocity and radius of each sphere. Approximately 10 to 20 falls for each parameter set were collected and use to generate plots of terminal velocity versus angle.
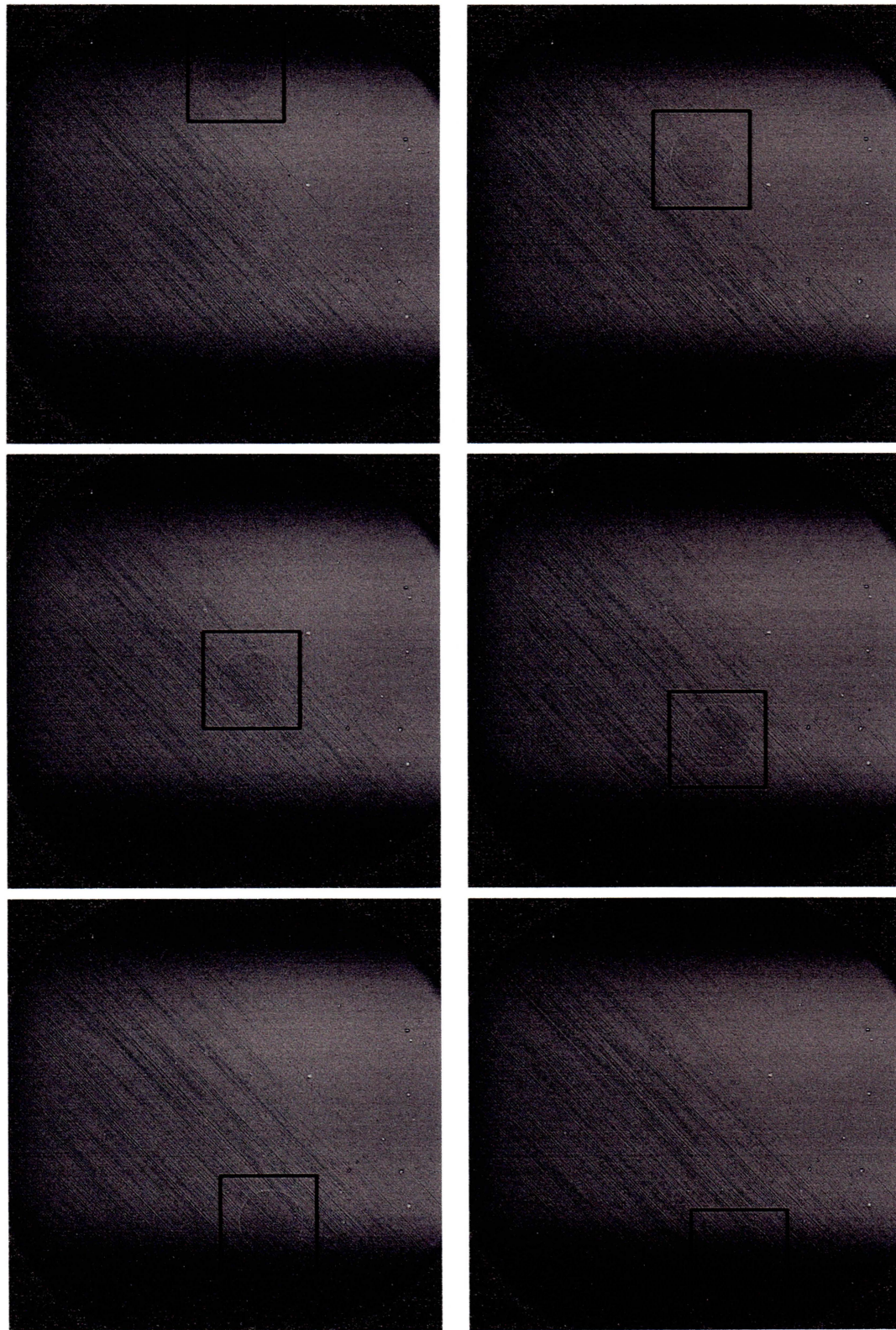
Figure 9: Time-lapse image sequence of a falling sphere through diluted EFH1 with PermC oriented at 47 degrees. The black squares are to locate the falling sphere.

3.4 Error Discussion

The remote actuator pushes the glass sphere out of the capillary tube from above the vial of ferrofluid. An air-ferrofluid interface must be penetrated by the sphere before its trajectory can be determined from data. This interface in certain cases caused a large deceleration of the particle causing most of the plotted trajectory to be in an accelerated state. In some cases the surface tension of the ferrofluid was large enough that the spheres would roll down the interface, imparting a horizontal component to its velocity that would carry it beyond the aperture of the camera. In certain cases the surface tension of the ferrofluid was so great that the spheres were unable to completely penetrate into the ferrofluid and would remain unsubmerged.

While loading the glass spheres into the capillary tubes some would become statically charged. This would cause an attraction between two or more spheres inside the capillary tube which would potentially cause multiple spheres to fall at the same time. Data from situations like these were not used as the results of Stokes flow around a sphere could not be used to on the non-spherical geometry. This led to many drops needing to be thrown away, reducing the amount of available data for study.

At times an electromagnet was used to generate the magnetic field and other times assemblies of permanent magnets were used. While a gaussmeter was used to measure the magnetic field and determine that it was relatively constant over the length scale of the experiment it was difficult to align due to the size of the experiment. This could cause a magnetic field gradient to appear over length of the experiment which would impose a force on the glass sphere, altering its trajectory. These effects were ignored for the respective experimental setups.

4 Results

4.1 Experimental Results

4.1.1 Angle-Dependence

Data analysis yielded results indicative of the presence of threads within the diluted ferrofluid. An upward trend can be seen in figure 10 of the terminal velocity of the falling sphere as angle α increases from horizontal, $\alpha = 0°$, to vertical, $\alpha = 90°$ with $\alpha = 100°$ corresponding to nonmagnetized ferrofluid. The increase of the average terminal velocity at each angle is both nonlinear and nonmonotonic. There is no reason to assume a linear increase in drag as the applied field angle is changed as the Shliomis model predicts angular variations as $\sin^2 \theta$, however the data for $\alpha = 36°$ has a much lower than expected terminal velocity, lower than that of $\alpha = 0°$. It is to be noted that an anomoly such as this did not occur for any other set of parameters; for magnetized ferrofluid minimal terminal velocity (maximal drag) was achieved when $\alpha = 0°$ and maximal terminal velocity (minimal drag) was achieved when $\alpha = 90°$.

Magnetic setups PermB and PermC have very similar effects on dilute EFH1 as shown in figure 11. This is a clear indication that magnetic saturation has been achieved within the ferrofluid and that there is no need to continue using PermB in further experiments analyzing magnetoviscous effects in 4:1 dilutions of EFH1.

In addition to the angle-dependent drag seen in the ferrofluid, upon double purification the drag increases in the ferrofluid lost most of its angle-dependence shown in figure 12. This is indicative of the larger nanoparticles being responsible for the
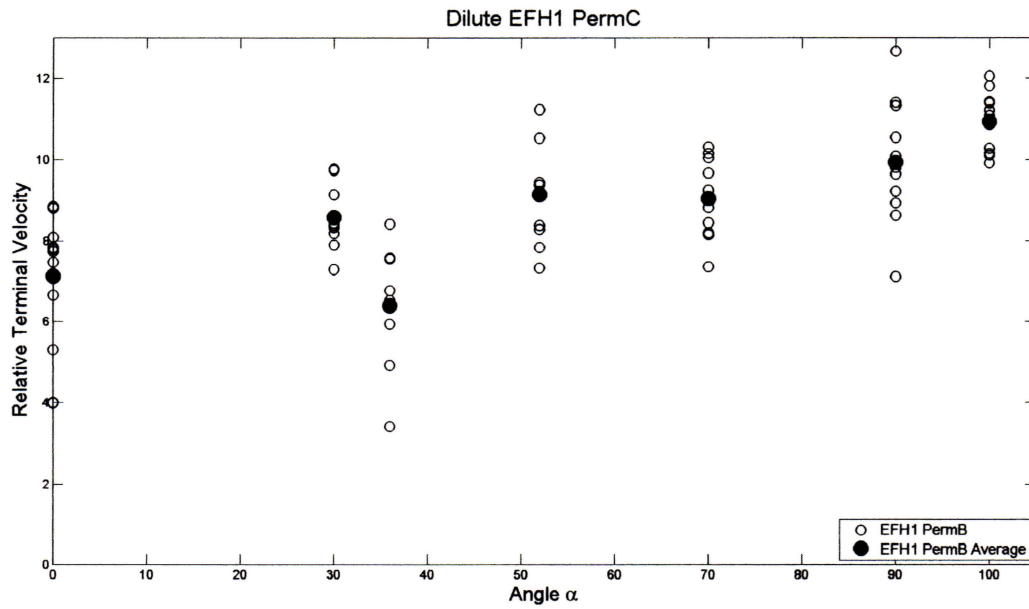
Figure 10: There is a positive correlation between terminal velocity and applied field angle indicating that as angle increase, drag on the falling sphere decreases. Filled circles indicate the average terminal velocity for the falls at that particular field angle. Field angle $\alpha = 100°$ represents no applied field (nonmagnetized ferrofluid).
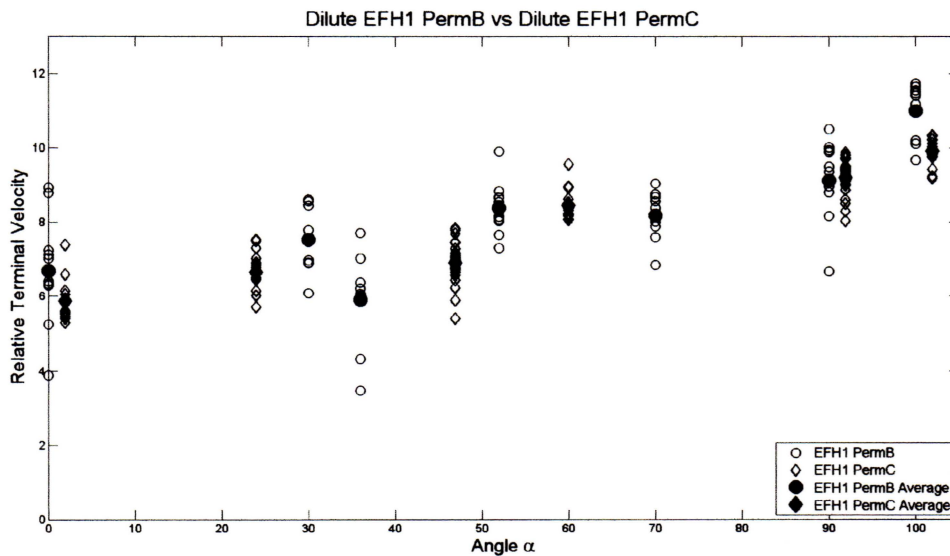
Figure 11: The relative increase in terminal velocity between ferrofluids magnetized by PermB and PermC are comparable. This indicates that magnetic saturation has been achieved through the PermC magnets (490 guass)
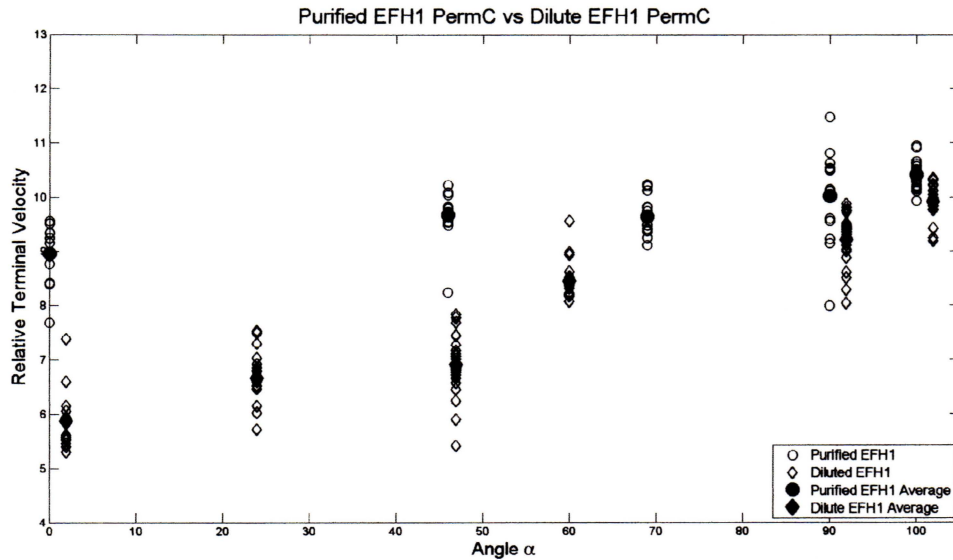
Figure 12: Upon double purification the angle-dependence of the terminal velocity seen in dilute EFH1 is reduced significantly, indicating a reduction in the number or strength of threads that form in the magnetized ferrofluid. The loss of angle dependence after the removal of the larger magnetic nanoparticles is indicative of larger particles being an important factor in the formation of thread-like macrostructures.

threading. By drawing out only the smaller particles with the ferrofluid, the doubly purified ferrofluid was unable to form many substantial threads and as such there was minimal interaction with the fluid envelope and the thread array, nearly removing all of the previously seen angle-dependence.

A closer look into the images and videos collected showed that there were striations across the screen that always aligned themselves with the applied magnetic field angle as in figure 13. In a few frames it was seen that the falling sphere was actually interacting with these striations and causing them to bend. Data analysis implies that these striations are the threads that are predicted to form inside diluted ferrofluids.

4.1.2 Data Precision

There is a large variance in the data presented in figure 10. In order to scale the terminal velocities and reduce the variance, the relationship between terminal

(a) Threads

(b) Bubble-thread Interaction
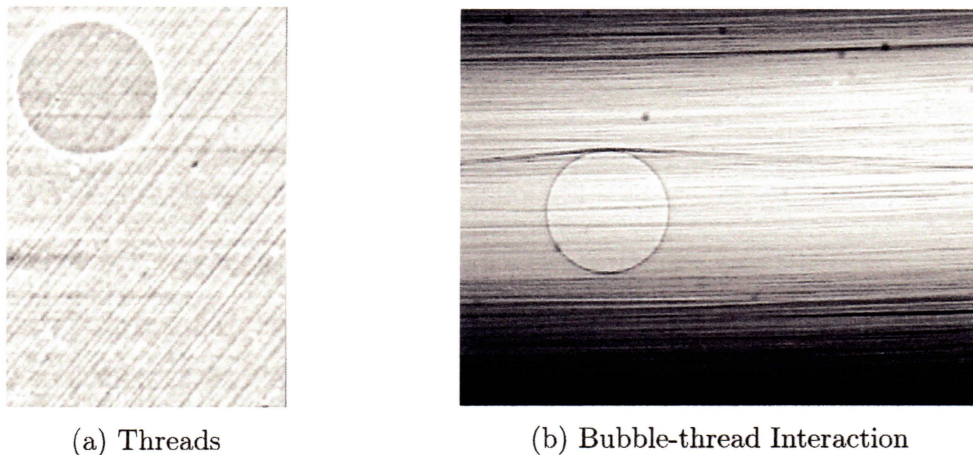
Figure 13: Images establishing existence of macro-structure threads and thread interactions. Threads are seen to span the entire container and are always aligned with the applied magnetic field. Sphere-thread interactions are very rare though there are some interactions as seen by the rising bubble in 13b.

velocity and falling sphere size is explored. Newton's second law is

$$\Sigma \boldsymbol{F} = m\boldsymbol{a}. \tag{27}$$

The two forces acting on a falling sphere are gravity and Stokes drag. By definition, terminal velocity occurs when the acceleration becomes zero. After using the relation $m = V\rho$ and equation (26), equation (27) now becomes

$$6\pi\mu r U_0 - \frac{4}{3}\pi r^3 \rho g = 0. \tag{28}$$

Solving for the terminal velocity, U_0 yields the equation

$$U_0 = \frac{2}{9}\frac{\rho g}{\mu}r^2. \tag{29}$$

As the density of the object does not change during motion, and terminal velocity is measured for a constant angle which is associated with a particular viscosity, it can be stated that terminal velocity is propotional to the radius of the falling sphere
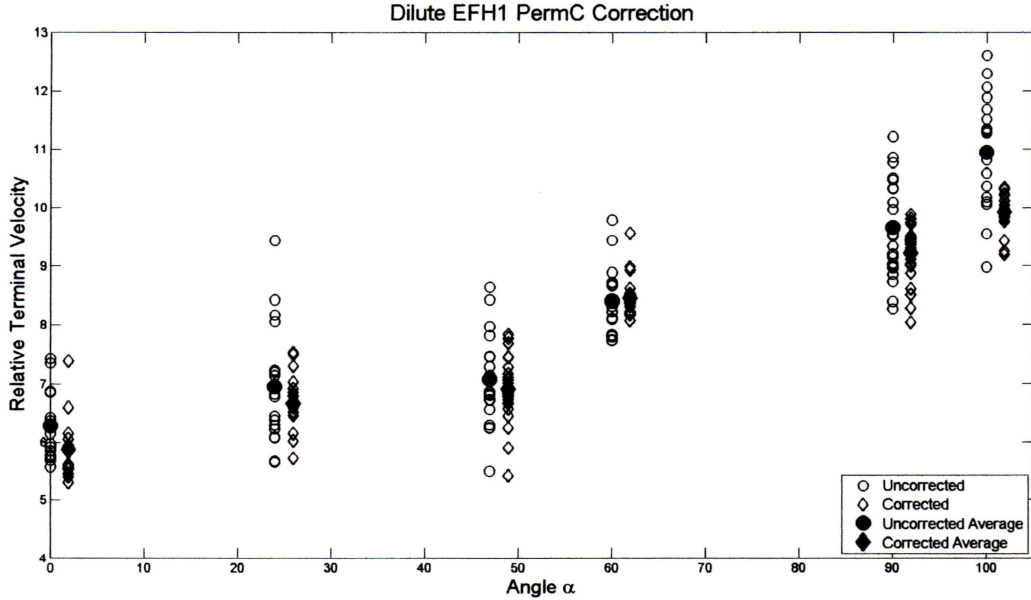
Figure 14: Variance reduction of dilute EFH1 under magnetic setup PermC

squared.

For each set of experimental parameters (angle, dilution, field strength) the radius of the falling sphere of each drop is recorded. The scale factor to adjust the terminal velocity of each falling sphere is the listed radius of all spheres squared (in pixels) divided by the recorded radius of each fall, or $\frac{R_0^2}{R^2}$ where R is an individual sphere's radius and R_0 is the listed radius of spheres used. The results of applying this scale factor can be seen in figures 14 and15.

4.2 Mathematical Model

Due to the lack of interaction between the sphere and the threads in the ferrofluid (figure 13a) and because we are operating in the Stokes regime, the proposed model is that the drag is a result of the interaction between the fluid envelope dragged along the falling sphere and the array of threads. Combining both the fact that ferrofluids have a low concentration of magnetic nanoparticles and that the ferrofluid was diluted 4:1, the volume fraction of threads in dilute EFH1 approaches zero. As demonstrated
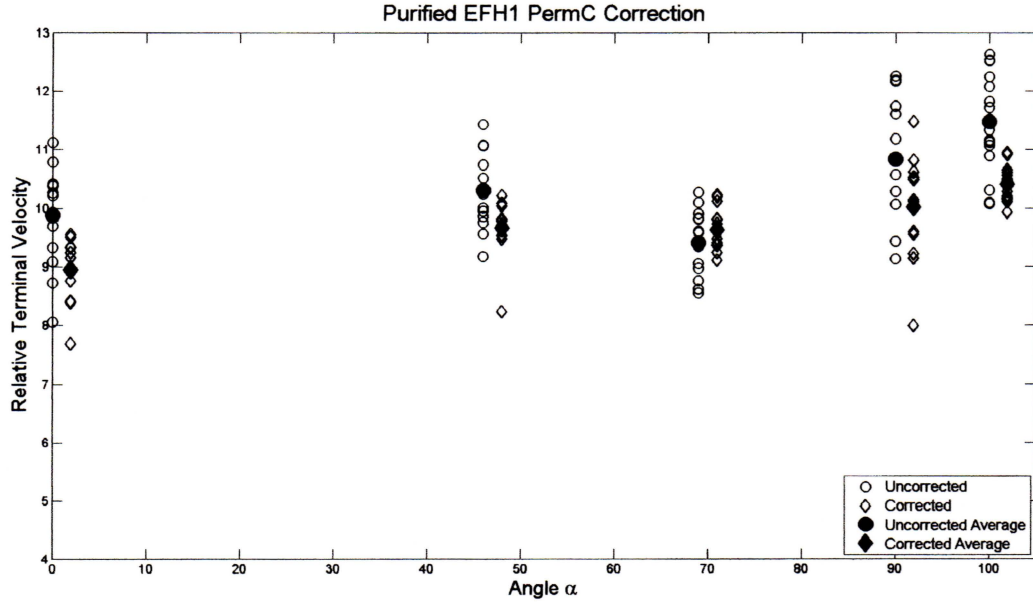
Figure 15: Variance reduction of purified EFH1 under magnetic setup PermC

by Happel, when the volume fraction tends to zero, an array of threads can be treated identically to a superposition of many individual non-interacting threads where the drag experienced by fluid flow normal to the thread's axis of symmetry is twice that of the fluid flow tangential to the thread's axis of symmetry.

Though cell models were the inspiration for this model, this model is not a cell model. Using the same assumption that the distance between threads is large enough that the flow disturbance by one thread fades by the time the next thread is reached, the total drag is simply the sum of the drag across every thread in the array. The global flow velocity obtained from equation (46) does not need to be altered due to the large spacing.

4.2.1 Directional Dependence

Banks demonstrated that in Stokes flow the drag experienced by fluid flow at an oblique angle through an array of thin, parallel fibers can be described by a linear combination of flow normal and tangential to the thread [27]. The drag can then be

written

$$\boldsymbol{f} = -\left[\tau(\boldsymbol{u} \cdot \hat{\boldsymbol{t}})\hat{\boldsymbol{t}} + \nu(\boldsymbol{u} - (\boldsymbol{u} \cdot \hat{\boldsymbol{t}})\hat{\boldsymbol{t}})\right] \tag{30}$$

where

$$\tau = \frac{2\pi\mu(1-c)^2}{Ku}$$

$$\nu = \frac{2\tau}{1-c}$$

$$\hat{\boldsymbol{t}} = \text{unit vector along direction of threads} \tag{31}$$

$$c = \text{volume fraction of threads}$$

$$Ku = \text{Kuwabara constant.}$$

The parameters τ and ν represent drag parameters for flow tangential and flow normal to the threads respectively, accounting for thread spacing. The Kuwabara constant, Ku, is defined by

$$Ku = c - \frac{1}{2}\ln c - \frac{3}{4} - \frac{1}{4}c^2, \tag{32}$$

and is a geometric factor that describes the amount of free space in the array [27]. The unit vector, $\hat{\boldsymbol{t}}$, is most easily described by in Cartesian coordinates by

$$\hat{\boldsymbol{t}} = \cos\alpha \, \hat{\boldsymbol{i}} + \sin\alpha \, \hat{\boldsymbol{k}} \tag{33}$$

as seen in figure 16. The unit vectors $\hat{\boldsymbol{i}}$ and $\hat{\boldsymbol{k}}$ correspond to the x and y axes respectively and are converted to spherical coordinates prior to performing drag computations.

The total drag in the flow around a sphere is the integral of the drag along the flow over the space around the sphere,

$$\int_V f \, dV \tag{34}$$
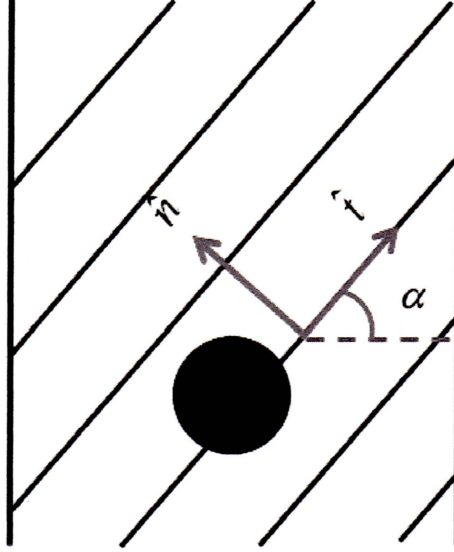
Figure 16: Schematic showing the thread unit vectors $\hat{n}$ and $\hat{t}$ tangential which are normal and tangential to the threads respectively, at angle α.

where $f = |\boldsymbol{f} \cdot \boldsymbol{u}|$ and dV is the volume element in spherical coordinates. Equation (30) can be manipulated into the form

$$\boldsymbol{f} = - \left[\nu \boldsymbol{u} + (\tau - \nu)(\boldsymbol{u} \cdot \hat{\boldsymbol{t}})\hat{\boldsymbol{t}} \right]. \tag{35}$$

The ferrofluids involved in the experiment are diluted, reducing the already low volume concentration of magnetic nanoparticles. Standard EFH1 ferrofluid has a volume fraction of magnetic nanoparticles in the range of 0.03 to 0.15 [30], which upon dilution yields a range of 0.006 to 0.03. After algebraic manipulation and the assumption that $c \to 0$, f now becomes

$$f = \tau(2|\boldsymbol{u}|^2 - (\boldsymbol{u} \cdot \hat{\boldsymbol{t}})^2). \tag{36}$$

4.2.2 Wall Effects

The models being explored up until now all made an assumption dealing with the flow at infinity. In the experiment and in the potential biomedical applications

the ferrofluid is confined to a finite cylindrical boundary. This confinement leads to an increase in drag, an effect know as the wall effect. [17, 31]. The strength of the wall effect is dependent upon the relative size of the falling sphere to the cylinder which will be described by the parameter λ throughout the rest of this thesis. For large values of λ large wall corrections are necessary to determine the proper amount of drag experienced by the falling sphere during its descent.

4.2.2.1   Approximate Stream Function

Generating stream plots and vector plots for Stokes flow around a sphere in an infinite medium is a simple task since the Stokes stream function is well-known. What is necessary is a stream function for flow around a sphere inside a cylinder. An approximate stream function for stokes flow past a sphere in an infinitely long cylinder that is falling directly down the center of the cylinder was derived by Haberman et al. [31]. Beginning with Stokes flow around a sphere viewed from the ball frame, the new boundary conditions of the flow are

$$\frac{\partial u}{\partial x} = -U_0, \quad \frac{\partial u}{\partial \rho} = 0 \qquad \text{when} \quad \rho = b$$

$$\frac{\partial u}{\partial x} = -U_0, \quad \frac{\partial u}{\partial \rho} = 0 \qquad \text{when} \quad x \to \infty \qquad (37)$$

$$\frac{\partial u}{\partial r} = 0, \quad \frac{\partial u}{\partial \theta} = 0 \qquad \text{when} \quad r = R$$

where x and ρ are the axial and radial coordinates in cylindrical coordinates respectively, r and θ are the radial and polar coordinates in spherical coordinates respectively, and b and R are the cylinder radius and sphere radius respectively. The boundary conditions on the cylinder are evaluated in cylindrical coordinates, transformed into spherical coordinates, and matched term-wise to the stream function derived in spherical coordinates. The boundary conditions of the sphere are evaluated in spherical coordinates and through substitution of the solution on the cylinder boundary conditions into the expression for the boundary condition on the sphere yields

an infinite set of equations whose solution fits the stream function to the boundary conditions. The approximate stream function for Stokes flow around a sphere falling inside of a cylinder is of the form

$$\psi_{approx} = C_2^{-1/2}(\cos\theta)\left(A_2 r^2 + B_2\frac{1}{r} + C_2 r^4 + D_2 r\right) + C_4^{-1/2}(\cos\theta)\left(A_4 r^4 + C_4 r^6\right)$$

(38)

where

$$\begin{aligned}
A_n =& (-1)^{\frac{n}{2}+1}\frac{1}{R^{n-2}}\left\{\left[\frac{1}{(n-2)!}S_3^{n-1} + \frac{n(n-1)}{(n-2)!(2n-3)}S_4^{n-2}\right]\frac{b_0}{R}\lambda^{n-1}\right.\\
&\left. + \left[-\frac{1}{(n-2)!}S_4^n + \frac{1}{(n-4)!(2n-3)}S_2^{n-1}\right]\frac{a_1}{R}\lambda^{n+1}\right\}
\end{aligned}$$

$$B_2 = a_1\pi$$

(39)

$$C_n = (-1)^{\frac{n}{2}+1}\frac{1}{R^n}\frac{1}{(n-2)!(2n+1)}\left(\frac{a_1}{R^3}S_2^{n+1}\lambda^{n+3} + \frac{b_0}{R}S_4^n\lambda^{n+1}\right)$$

$$D_2 = b_0\pi.$$

$C_n^{-1/2}(t)$: Gegenbauer polynomial

In the above equations, a_1 and b_0 are the first constants from the infinite set of equations, λ is the ratio of the sphere radius to the cylinder radius, and the values of S_i^j are given in a table on page 56 of [31].

4.2.2.2 Nondimensionalization

The stream function ψ_{approx} has two main parameters that need to be altered: the ball radius, R, and the cylinder radius, b. Through nondimensionalization these two parameters can be reduced to where the only parameter is λ. Fully expanded, the

approximate stream function as seen from the ball frame is

$$
\begin{aligned}
\psi(r,\theta) = {} & \frac{1}{2}(1-\cos^2\theta)\left(\left(-4.40866\frac{b_0}{R}\lambda - 6.55507\frac{a_1}{R^3}\lambda^3 + U_0\right)r^2 + \left(a_1\pi\right)\frac{1}{r}\right. \\
& \left. + \left(1.31101\frac{b_0}{R^3}\lambda^3 + 3.57466\frac{a_1}{R^5}\lambda^5\right)r^4 + \left(b_0\pi\right)r\right) \\
& + \frac{1}{8}(1-\cos^2\theta)(5\cos^2\theta - 1)\left(\left(1.07057\frac{b_0}{R^3}\lambda^3 - 4.07724\frac{a_1}{R^5}\lambda^5\right)r^4\right. \\
& \left. - \left(0.850256\frac{b_0}{R^5}\lambda^5 + 3.36589\frac{a_1}{R^7}\lambda^7\right)r^6\right)
\end{aligned}
\tag{40}
$$

where the quantities $\frac{b_0}{R}$ and $\frac{a_1}{R^3}$ are given by

$$
\frac{b_0}{R} = -\frac{3U_0}{2\pi}\frac{1-0.75875\lambda^5}{1-2.1050\lambda + 2.0865\lambda^3 - 1.7068\lambda^5 + 0.72603\lambda^6}
\tag{41}
$$

$$
\frac{a_1}{R^3} = \frac{-\frac{b_0}{R}\left(\frac{5}{2}\pi - 6.55507\lambda^3\right)}{\frac{15}{2}\pi - 17.8733\lambda^5}
\tag{42}
$$

Nondimensionalization of equation (40) yields

$$
\begin{aligned}
\psi(r,\theta) = {} & \frac{1}{2}(1-\cos^2\theta)\left(\left(-4.40866\frac{b_0}{R}\lambda - 6.55507\frac{a_1}{R^3}\lambda^3 + 1\right)r^2 + \left(\frac{a_1}{R^3}\lambda^3\pi\right)\frac{1}{r}\right. \\
& \left. + \left(1.31101\frac{b_0}{R}\lambda + 3.57466\frac{a_1}{R^3}\lambda^3\right)r^4 + \left(\frac{b_0}{R}\lambda\pi\right)r\right) \\
& + \frac{1}{8}(1-\cos^2\theta)(5\cos^2\theta - 1)\left(\left(1.07057\frac{b_0}{R}\lambda - 4.07724\frac{a_1}{R^3}\lambda^3\right)r^4\right. \\
& \left. - \left(0.850256\frac{b_0}{R}\lambda + 3.36589\frac{a_1}{R^3}\lambda^3\right)r^6\right).
\end{aligned}
\tag{43}
$$

The experimental value of λ is 0.106 in which case $\lambda \ll 1$ indicating that higher order powers of λ can be discarded. Taking the powers λ^2 and higher to be zero, the

nondimensional forms of equations (41) and (42) can be written as

$$\frac{b_0}{R} = -\frac{3}{2\pi}\frac{1}{1 - 2.1050\lambda} = -\frac{3}{2\pi}(1 + 2.105\lambda + 2.105^2\lambda^2 + \dots) \tag{44}$$

$$\frac{a_1}{R^3} = \frac{1}{2\pi}\frac{1}{1 - 2.1050\lambda} = \frac{1}{2\pi}(1 + 2.105\lambda + 2.105^2\lambda^2 + \dots) \tag{45}$$

By substituting equations (44) and (45) into equation (43) one obtains the nondimensional stream function

$$
\begin{aligned}
\psi(r,\theta) = \frac{1}{2}(1 - \cos^2\theta) &\left\{ \left[-4.40866\left(-\frac{3}{2\pi}\left(\lambda + 2.105\lambda^2 + 2.105^2\lambda^3 + \dots\right)\right) \right.\right. \\
&\left. -6.55507\frac{1}{2\pi}\left(\lambda^3 + 2.105\lambda^4 + 2.105^2\lambda^5 + \dots\right) + 1\right] r^2 \\
&+ \left[\frac{1}{2\pi}(\lambda^3 + 2.105\lambda^4 + 2.105^2\lambda^5 + \dots)\pi\right]\frac{1}{r} \\
&+ \left[1.31101\left(-\frac{3}{2\pi}\left(\lambda + 2.105\lambda^2 + 2.105^2\lambda^3 + \dots\right)\right)\right. \\
&\left.+3.57466\frac{1}{2\pi}\left(\lambda^3 + 2.105\lambda^4 + 2.105^2\lambda^5 + \dots\right)\right] r^4 \\
&\left.+ \left[-\frac{3}{2\pi}\left(\lambda + 2.105\lambda^2 + 2.105^2\lambda^3 + \dots\right)\pi\right] r\right. \\
+\frac{1}{4}(5\cos^2\theta - 1) &\left(\left[1.07057\left(-\frac{3}{2\pi}\left(\lambda + 2.105\lambda^2 + 2.105^2\lambda^3 + \dots\right)\right)\right.\right. \\
&\left. -4.07724\frac{1}{2\pi}\left(\lambda^3 + 2.105\lambda^4 + 2.105^2\lambda^5 + \dots\right)\right] r^4 \\
&- \left[0.850256\left(-\frac{3}{2\pi}\left(\lambda + 2.105\lambda^2 + 2.105^2\lambda^3 + \dots\right)\right)\right. \\
&\left.\left.\left. +3.36589\frac{1}{2\pi}\left(\lambda^3 + 2.105\lambda^4 + 2.105^2\lambda^5 + \dots\right)\right] r^6\right)\right\}.
\end{aligned}
\tag{46}
$$

4.2.2.3   Region of Validity

This stream function works well when $r < 1$, however for $r > 1$ the value of ψ increases without bounds. This is neither desired nor physically accurate. It is not easily seen if there is a particular region where higher order terms of λ can be thrown away. Resolving equation (46) in terms of λ may help discard some of the higher order

terms. After factoring out $\frac{1}{2\pi}\sin^2\theta$, distributing, and grouping based upon powers of λ one has

$$
\begin{aligned}
\psi(r,\theta) = \frac{1}{4\pi}\sin^2\theta\Bigg\{ &\left[-3\pi r + 13.00598r^2 - \left(3.93303 + 0.80293\left(5\cos^2\theta - 1\right)\right)r^4\right. \\
&\left. + 0.63769\left(\left(5\cos^2\theta - 1\right)r^6\right]\lambda\right. \\
&+ \left[-3\pi r + 27.84069r^2 - \left(8.27903 + 1.69017\left(5\cos^2\theta - 1\right)\right)r^4\right. \\
&\left. + 1.34234\left(5\cos^2\theta - 1\right)r^6\right]\lambda^2 \\
&+ \left[\pi\frac{1}{r} - 13.23908\pi r + 52.04958r^2 + \left(13.85269 + 4.57710\left(5\cos^2\theta - 1\right)\right)r^4\right. \\
&\left. + 7.93663\left(5\cos^2\theta - 1\right)r^6\right]\lambda^3 \\
&+ \left[2.105\pi\frac{1}{r} - 13.79842r^2 + \left(7.52466 - 2.14565\left(5\cos^2\theta - 1\right)\right)r^4\right. \\
&\left. - 1.77130\left(5\cos^2\theta - 1\right)r^6\right]\lambda^4 \\
&+ \left[4.43103\pi\frac{1}{r} - 29.04567r^2 + \left(15.83941 - 4.51659\left(5\cos^2\theta - 1\right)\right)r^4\right. \\
&\left. - 3.72859\left(5\cos^2\theta - 1\right)r^6\right]\lambda^5 + 2\pi r^2\Bigg\}.
\end{aligned}
$$

$$(47)$$

In order to fit the shape of a cylinder, the angle θ must be constrained for certain values of r. When $r \le 1$, the angle θ remains unconstrained, however when $r > 1$, the maximum angle θ can take is $\theta = \sin^{-1}\frac{1}{r}$. For large r, $\sin^2\theta$ is small but does not go to zero quickly enough to cancel the growth of higher order terms of r. As λ is the small parameter in the expansion, for the stream function to be applicable for $r > 1$ the coefficients of λ must be of order 1. This is not true when $r > 1$ and as a result, the approximate stream function in equation (46) can only be used to integrate up to a radius equal to that of the cylinder wall, $r = 1$.

4.2.2.4 Results

The mathematical model was tested using Mathematica. In figures 17 and 18,

(a) Ball Frame   (b) Lab Frame
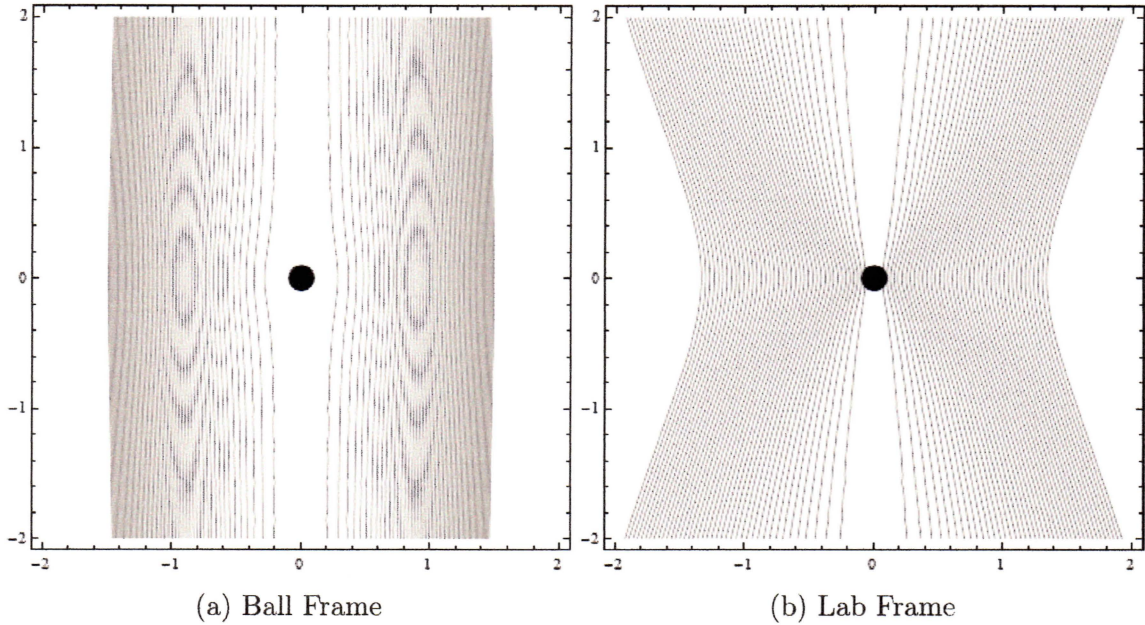
Figure 17: Stream function isolines of flow in an infinite medium around a sphere of radius $R = \lambda = 0.1$ Streamlines in the ball frame wrap around the sphere and slowly straighten out to uniform flow. Streamlines in the Lab frame meet the sphere's surface and curve away.

(a) Ball Frame   (b) Lab Frame

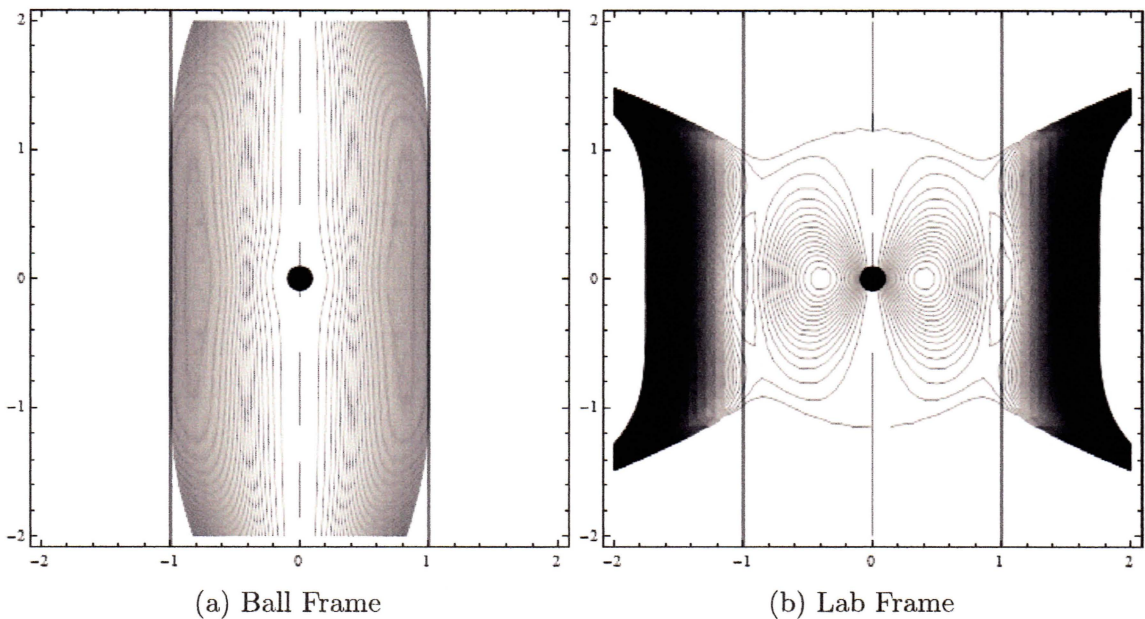Figure 18: Approximate stream function in an infinite cylinder with $R = \lambda = 0.1$ Streamlines in the ball frame act similarly to that of uniform flow until $r \gg 1$ where the streamlines begin to turn inwards at the top and bottom of the cylinder. Streamlines in the lab frame turn back and terminate on the cylinder walls until $r > 1$ when streamlines then violate the boundary conditions specified in equation (37).
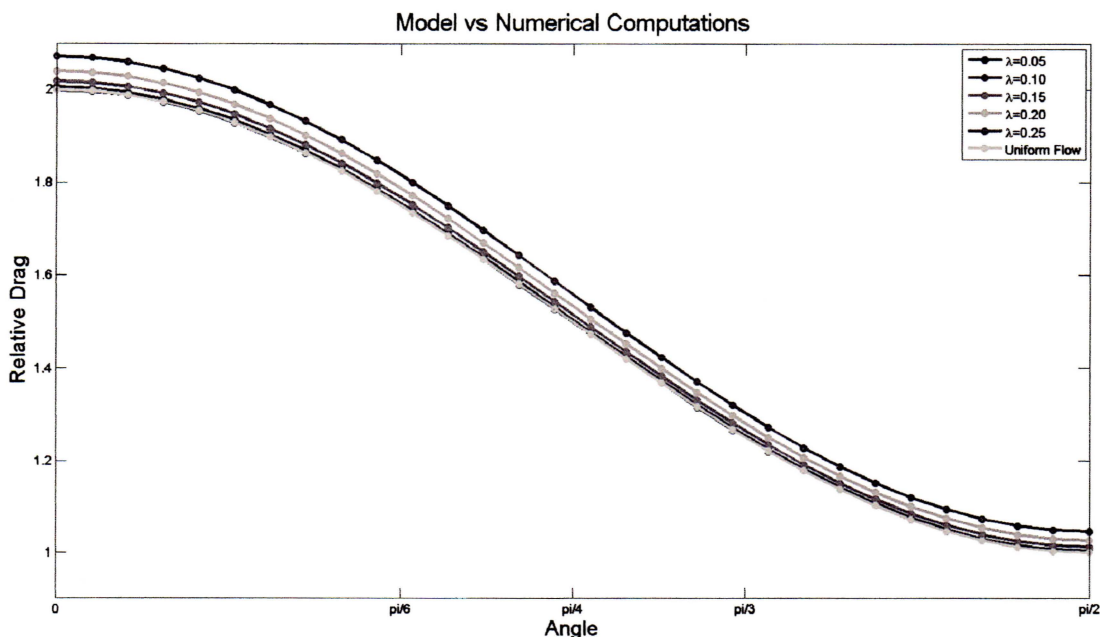
Figure 19: Model results for multiple values of λ. Each λ was scaled by the maximum drag of $\lambda = 0.01$ and plotted with the uniform flow model. The drag profile is unchanged as λ is varied, implying that sphere radius is the primary source of drag on the sphere, not the flow velocity or the walls.

Stream plots are provided to compare the qualitative differences between the standard Stokes flow around a sphere and the approximate stream function's flow around a sphere in a cylinder. Far from the sphere, the approximate stream function begins to deviate. In figure 18b the stream lines behave properly until the cylinder wall is reached, as indicated by equation (47). Beyond that in all directions the stream function produces streamlines in invalid regions, such as flows outside of the cylinder.

Model results are given in figure 19. Maximal drag is seen when the sphere is falling through a perpendicular applied field and minimal when the direction of motion and the applied field are parallel. In the limit as $\lambda \to 0$, the model produces the same curve as that of uniform flow. As λ increases, so does the amount of drag experienced by the sphere across all angles of applied field. This can be interpreted by recalling that the speed of the falling sphere varies like the square of the radius of the sphere from equation (29). Since the radius varies as λ and drag varies as speed it now
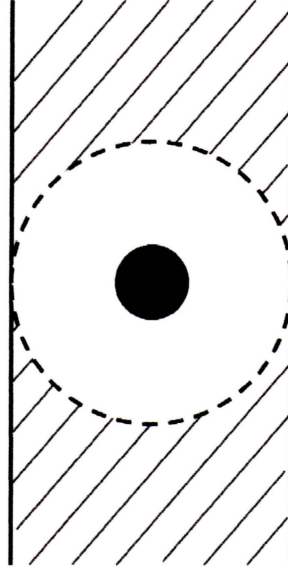
44

Figure 20: The region of integration is confined to the sphere of radius $r = 1$. The shaded region outside of the dotted circle is not integrated by the model and could have an impact on the drag profile seen in figure 19.

becomes apparent that this should be the case.

5   Discussion and Conclusions

In dilute, magnetized ferrofluids, particle aggregates occur that take the form of long, thin cylindrical structures. These structures behave in accordance to slender body theory in that flow perpendicular to the axis of symmetry of the structure will produce twice as much drag as flow oriented parallel to the structure's axis of symmetry. Even though these structures form an array throughout the experiment, in the limit of small magnetic pariticle concentrations, a thread array behaves identically to a single thread.

As can be seen from the experimental results and the captured images these threads are the dominant source of drag in this experiment; maximal drag is achieved as the sphere falls perpendicular to the applied field. This does not imply that Shliomis- and de Gennes-predicted drags do not occur in these samples, only that

they are dominated by the effect of the threads. A mathematical model is created that assumes all drag to come from the interaction of the fluid envelope dragged by the falling sphere with the threads with no contributions from sphere-thread interactions due to the infrequency with which such collisions were observed.

A model was created that calculates the drag experienced by a falling sphere through thread arrays in magnetized ferrofluid by assuming that in the limit of small volume concentration of magnetic nanoparticles the distance between threads would be large enough that the effects of one thread on the flow would not persist long enough to affect another thread. With this assumption the total drag was calculated as the sum of the drag caused by each individual thread in the array. The model recovers uniform flow when λ approaches zero and finds increasing drag as λ is increased. The drag profiles are similar regardless of the sphere radius, implying that flow around the sphere and the walls are not major contributors to the drag experienced by the flow; the most important factor in the increase in drag is the size of the falling sphere.

The model in figure 19 was not integrated over all space; r is confined to the interval $[\lambda \ 1]$ as determined by the analysis of section 4.2.2.3. In terms of the vial used in the experiment, an equal amount of volume was left unintegrated as was integrated by the model. Since the model is unable to integrate the shaded section of figure 20 it is unknown whether or not the flow outside of the sphere of $r = 1$ will have any large impact on the total drag experienced by the falling sphere.

References

[1] J. Popplewell, "Technological applications of ferrofluids," *Phys. Technol.*, vol. 15, pp. 150–156, 1984.

[2] S. Odenbach, "Recent progress in magnetic fluid research," *Journal of Physics: Condensed Matter*, vol. 16, pp. R1135–R1150, 2004.

[3] A. Nacev, C. Beni, O. Bruno, and B. Shapiro, "Magnetic nanoparticle transport within flowing blood and into surrounding tissue," *Nanomedicine*, vol. 5, no. 9, pp. 1459–1466, 2010.

[4] J. Nowak, D. Wolf, and S. Odenbach, "A rheological and microscopial characterization of biocompatible ferrofluids," *Journal of Magnetism and Magnetic Materials*, vol. 354, pp. 174–177, November 2014.

[5] D. J. Griffiths, *Introduction to Electrodynamics*. Prentice-Hall Inc., 3 ed., 1999.

[6] M. I. Shliomis, "Effective viscosity of magnetic suspensions," *Soviet Physics JETP*, vol. 34, pp. 1291–1294, June 1972.

[7] P. G. de Gennes and P. A. Pincus, "Pair correlations in a ferromagnetic colloid," *Phys. kondens. Materie*, vol. 11, pp. 189–198, 1970.

[8] W.-k. Lee, "X-ray microtomography of field-induced macro-structures in a ferrofluid," *Journal of Magnetism and Magnetic Materials*, vol. 322, pp. 2525–2528, March 2010.

[9] A. Y. Zubarev and L. Y. Iskakova, "Yield stress in thin layers of ferrofluids," *Physica A*, vol. 365, pp. 265–281, 2006.

[10] A. Y. Zubarev and L. Y. Iskakova, "On the theory of rheological properties of magnetic suspensions," *Physica A*, vol. 382, pp. 378–388, 2007.

[11] L. M. Pop, S. Odenbach, A. Wiedenmann, N. Matoussevitch, and H. Bönnemann, "Microstructure and rheology of ferrofluids," *Journal of Magnetism and Magnetic Materials*, vol. 289, pp. 303–306, 2005.

[12] L. M. Pop and S. Odenbach, "Investigation of the microscopic reason for the magnetoviscous effect in ferrofluids studied by small angle neutron scattering," *Journal of Physics: Condensed Matter*, vol. 18, pp. S2785–S2802, September 2006.

[13] W.-K. Lee and J. Ilavsky, "Particle size distribution in ferrofluid macro-clusters," *Journal of Magnetism and Magnetic Materials*, vol. 330, pp. 31–36, October 2013.

[14] S. Thurm and S. Odenbach, "Particle size distribution as key parameter for the flow behavior of ferrofluids," *Physics of fluids*, vol. 15, pp. 1658–1664, June 2003.

[15] R. W. Chantrell, J. Sidhu, P. R. Bissell, and P. A. Bates, "Dilution induced instability in ferrofluids," *Journal of Applied Physics*, vol. 53, pp. 8341–8343, November 1982.

[16] Ferrotec Corporation, "Ferrotec EFH series education ferrofluid type: EFH1." `https://www.ferrotec.com/index.php?id=audioFluid&vfp_id=125`, June 2014.

[17] J. Happel and B. Byrne, "Motion of a sphere and fluid in a cylindrical tube," *Industrial and Engineering Chemistry*, vol. 46, pp. 1181–1187, June 1954.

[18] S. Childress, "An introduction to theoretical fluid dynamics." Lecture notes, February 2008.

[19] G. K. Batchelor, "Slender-body theory for particles of arbitrary cross-section in stokes flow," *Journal of Fluid Mechanics*, vol. 44, no. 3, pp. 419–440, 1970.

[20] R. G. Cox, "The motion of long slender bodies in a viscous fluid part 1. general theory," *Journal of Fluid Mechanics*, vol. 44, no. 4, pp. 791–810, 1970.

[21] H. Hasimoto, "On the periodic fundamental solutions of the stokes equations and their application to viscous flow past a cubic array of spheres," *Journal of Fluid Mechanics*, vol. 5, pp. 317–328, January 1959.

[22] E. Sparrow and A. Loeffler, "Longitudinal laminar flow between cylinders arranged in regular array," *A.I.Ch.E*, vol. 5, pp. 325–330, September 1959.

[23] H. Brinkman, "A calculation of the viscous force exerted by a flowing fluid on a dense swarm of particles," *Appl. Sci. Res.*, vol. A1, pp. 27–34, February 1947.

[24] S. Childress, "Viscous flow past a random array of threads," *Journal of Chemical Physics*, vol. 56, pp. 2527–2539, March 1972.

[25] S. Kuwabara, "The forces experienced by randomly distributed parallel circular cylinders or spheres in a viscous flow at small reynolds numbers," *Journal of the Physical Society of Japan*, vol. 14, pp. 527–532, April 1959.

[26] J. Happel, "Viscous flow relative to arrays of cylinders," *A.I.Ch.E Journal*, vol. 5, pp. 174–177, June 1959.

[27] D. O. Banks, "Stokes flow through a system of parallel infinite cylinders with axes oriented at an angle to the direction of mean flow," *Particulate Science and Technology: An International Journal*, vol. 5, no. 3, pp. 339–353, 1987.

[28] P. K. Kundu and I. M. Cohen, *Fluid Mechanics*. Elsevier Inc., 4 ed., 2008.

[29] Q. L. Peng, S. M. McMurry, and J. M. D. Coey, "Axial magnetic field produced by axially and radially magnetized permanent rings," *Journal of Magnetism and Magnetic Materials*, vol. 268, pp. 165–169, 2003.

[30] Ferrotec Corporation, "Material safety data sheet." `https://www.ferrotec.com/downloads/efhmsds.pdf`, March 2009.

[31] W. L. Haberman and R. M. Sayre, "Motion of rigid and fluid spheres in stationary and moving liquids inside cylindrical tubes," Hydromechanics Laboratory Research and Development 1143, Department of the Navy, October 1958.
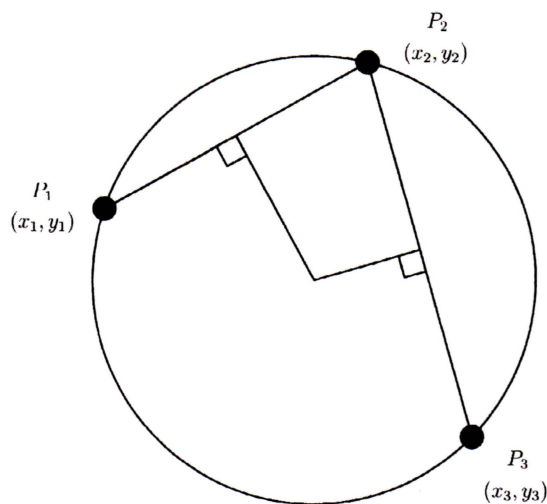
Figure 21: The midpoint of a circle can be derived by choosing three random points about its circumference. The perpendicular bisectors of the line segments $\overline{P_1 P_2}$ and $\overline{P_2 P_3}$ intersect at the center of the circle.

A   Excel

The midpoint along the line between points P_1 and P_2 is $\left(\frac{1}{2}(x_1 - x_2), \frac{1}{2}(y_1 - y_2)\right)$ and the slope of a perpendicular line is $m_{12} = -\frac{x_1 - x_2}{y_1 - y_2}$. The equation of the perpendicular bisector of $\overline{P_1 P_2}$ is

$$y_m = -\frac{x_1 - x_2}{y_1 - y_2} x_m + \frac{1}{2}\left(\frac{x_1^2 - x_2^2}{y_1 - y_2} + y_1 + y_2\right).$$

By the same logic, the perpendicular bisector of $\overline{P_1 P_3}$ is

$$y_m = -\frac{x_1 - x_3}{y_1 - y_3} x_m + \frac{1}{2}\left(\frac{x_1^2 - x_3^2}{y_1 - y_3} + y_1 + y_3\right).$$

Setting these two equations equal to each other and solving yields the expression.

$$x_m = \frac{\frac{1}{2}\left(\frac{x_1^2 - x_3^2}{y_1 - y_3} + y_1 + y_3 - \left(\frac{x_1^2 - x_2^2}{y_1 - y_2} + y_1 + y_2\right)\right)}{\frac{x_1 - x_3}{y_1 - y_3} - \frac{x_1 - x_2}{y_1 - y_2}}.$$